JGR Solid Earth

RESEARCH ARTICLE
10.1029/2020JB019862

Special Section:
Creep on continental faults and subduction zones: Geophysics, geology, and mechanics

Mixed-Mode Formation of Amorphous Materials in the Creeping Zone of the Chihshang Fault, Taiwan, and Implications for Deformation Style

Wen-Jie Wu[1], Li-Wei Kuo[1,2], Ching-Shun Ku[3], Ching-Yu Chiang[3], Hwo-Shuenn Sheu[3], Tyas Dwi Aprilniadi[1], and Jia-Jyun Dong[1,2,4]

[1]Department of Earth Sciences, National Central University, Taoyuan, Taiwan, [2]Earthquake-Disaster & Risk Evaluation and Management Center, National Central University, Taoyuan, Taiwan, [3]National Synchrotron Radiation Research Centrer, Hsinchu, Taiwan, [4]Graduate Institute of Applied Geology, National Central University, Taoyuan, Taiwan

Key Points:
- Amorphous materials (AMs), derived from shear-induced amorphization, were observed in the creeping Chihshang Fault, Taiwan
- AMs within a localized narrow band and along scaly clay fabrics can be treated brittle and ductile deformation in bulk fault rocks
- The presence of AMs was resulted from lasting on-fault amorphization driven by tectonic loading and stress relaxation

Correspondence to:
L.-W. Kuo,
liweikuo@ncu.edu.tw;
liweikuo@gmail.com

Citation:
Wu, W.-J., Kuo, L.-W., Ku, C.-S., Chiang, C.-Y., Sheu, H.-S., Aprilniadi, T. D., & Dong, J.-J. (2020). Mixed-mode formation of amorphous materials in the creeping zone of the Chihshang Fault, Taiwan, and implications for deformation style. *Journal of Geophysical Research: Solid Earth*, *125*, e2020JB019862. https://doi.org/10.1029/2020JB019862

Received 26 MAR 2020
Accepted 21 MAY 2020
Accepted article online 22 MAY 2020

Abstract Experimental results demonstrate that amorphous materials can be generated by frictional sliding at a wide range of conditions and that once formed the frictional strength of the fault is reduced. Nevertheless, amorphous materials have not been described in many natural faults, and their importance in natural systems is not well understood. We have identified amorphous materials within a 3-mm-thick slip zone (i.e., narrow band) in the Chihshang Fault, Taiwan, as well as within a submicrometer thick band in a distributed network of scaly clays. The scaly clays resemble those developed in other faults that demonstrably accommodated slow creep, and they also impart very low permeability implying that fluid-related alteration (which could result in amorphization) will be inefficient. For this reason, and because of its throughgoing nature and position within a deforming zone, we infer a shear-related origin for the amorphous materials. Therefore, amorphous materials can be observed in near-surface environments because they have been formed during recent deformation under limited fluid-circulation circumstances. The narrow slip zone containing amorphous materials is throughgoing and is interpreted to have acted as a frictional interface that accommodated brittle deformation at the macroscopic scale, whereas the surrounding mélange accommodated distributed "ductile" shear. The formation of amorphous materials therefore typifies the "mixed-mode" style of deformation in this creeping fault zone.

1. Introduction

Fault rocks develop due to a spectrum of deformation mechanisms and styles, ranging from localized brittle deformation to distributed ductile deformation, which produces distinct microstructures and phase changes at aseismic (i.e., slip velocities from 10^{-9} to 10^{-4} m/s; Ikari & Kopf, 2017) to seismic (i.e., slip velocities from 0.1 to 10 m/s; Heaton, 1990) strain rates. Amorphous materials (AMs) are one type of fault zone material that is rarely exposed in natural faults and difficult to directly observe. Nevertheless, pseudotachylytes (Di Toro et al., 2006), silica gel (Kirkpatrick et al., 2013), and fault mirrors (Kuo et al., 2016; Ohl et al., 2020) have been recognized as fault-related rocks containing AMs. It has been recognized that AMs can occur in faults and simulated creeping zones that formed at aseismic deformation conditions (Janssen et al., 2010; Pec et al., 2012). In addition to the AMs generated by faulting, AMs could also be derived from chemical and bacterial weathering at shallow depths (Hellmann et al., 2012; Potysz et al., 2016). Once formed, they are a metastable phase that can be the precursor to the formation of clay minerals (Kawano & Tomita, 1996; Kuo et al., 2009).

By investigating deformed fault rocks in the slip zones of natural and experimental faults, a range of mechanochemical processes has been recognized as important in mineral amorphization, including frictional melting (Di Toro et al., 2006; Sibson, 1975), comminution of clasts (Janssen et al., 2010; Ozawa & Takizawa, 2007; Pec et al., 2012, 2016; Toy et al., 2015; Wenk, 1978; Yund et al., 1990), and mechanically activated disassociation and subsequent precipitation of carbonaceous solids (Delle Piane et al., 2018). Recently, it was suggested that AMs may be responsible for fault lubrication and healing (Rowe et al., 2019).

Despite progress in understanding the role of AMs in fault mechanics, examples from within the slip zones of natural faults remain scarce, and the related mechanisms of formation are not well understood. Further

geological evidence, including the description of deformation textures and possible mechanisms of formation, is required to improve our understanding of the role that AMs have in controlling fault rheology during the seismic cycle. Here we report the first occurrence of AMs in the creeping zone of the Chihshang Fault in Taiwan. We obtain mineralogical and microstructural evidence by analyzing the AMs at submicron scale via high spatial resolution microscopic and diffraction methods. Based on our observations, we suggest that gouge amorphization is likely driven by on-fault deformation and the occurrences of AMs likely exhibit the deformation styles within the Chihshang Fault creeping zone. Because (1) amorphization processes on fault-zone materials can change the intrinsic physical properties of fault zones and (2) AMs can be altered to stable phases (e.g., smectite) through fluid-rock alteration, we suggest that gouge amorphization may alter the physicochemical characteristics of the fault zone and the strength of the fault during the seismic cycle.

2. Geological Setting and Methods

2.1. The Chihshang Fault and Samples

The Chihshang Fault is located in the southern part of the Longitudinal Valley Fault (LVF) at the present-day suture between the Eurasian and Philippine Sea Plates. The LVF separates the Central Range (deformed Chinese margin to the west) from the Coastal Range (the northernmost segment of the Luzon Arc to the east) (Figure 1b). Long-term geodetic observations indicate an oblique convergent velocity of ~82 mm/yr (Figure 1a) (Yu et al., 1997) and shortening of ~31 mm/yr across the Chihshang Fault (Lee et al., 2003). The shallow creeping segment of the Chihshang Fault lies within the Lichi Mélange in its hanging wall (Figure 1b) (Angelier et al., 2000; Lee et al., 2006; Thomas et al., 2014). The Chihshang Fault is an oblique thrust with a significant component of left-lateral strike-slip. It is the only active creeping

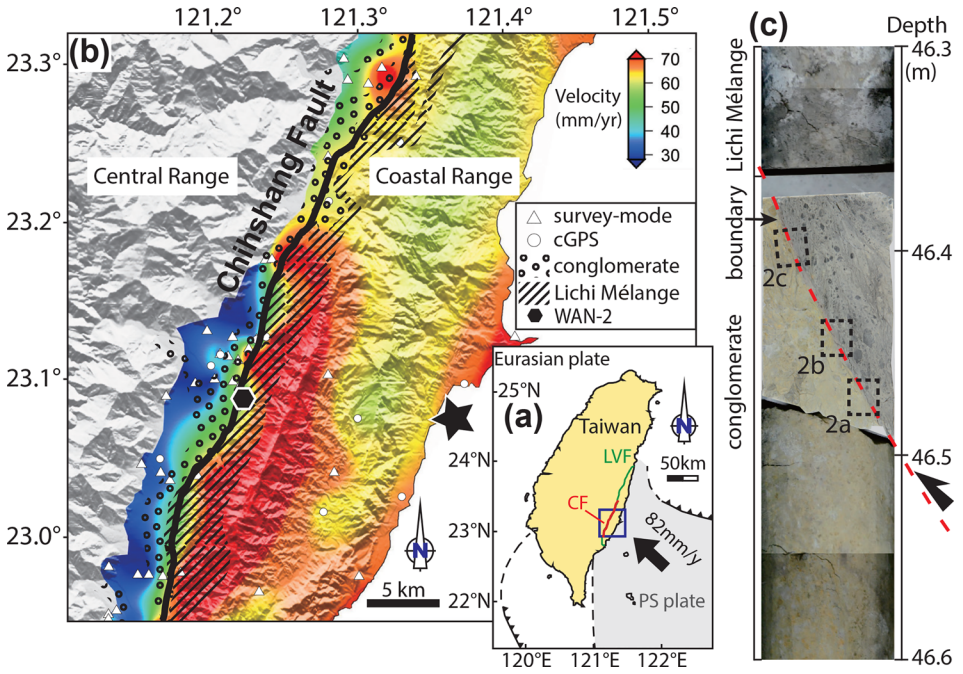

Figure 1. Geological and geodetic setting of the Chihshang Fault (CF) and location of the WAN-2 drilling site (the hexagon). (a) The Longitudinal Valley Fault (LVF) in eastern Taiwan as a plate boundary. LVF accommodates ~82 mm/yr of oblique convergent motion between the Philippine Sea Plate (PS plate) and the Eurasian plate. (b) Variation of the Global Positioning System (GPS) velocity field along the Chihshang Fault. GPS data collected from 2007 to 2015 (circles: continuous mode GPS, cGPS; triangles: survey mode GPS). Velocity contours show that the Chihshang Fault has accommodated shortening with horizontal deformation rates of ~30 mm/yr within the Lichi Mélange. The star indicates the epicenter of Chengkung earthquake in 2003. (c) Core images of the WAN-2 borehole and sampling positions of petrographic thin sections. The Lichi Mélange thrusted toward the conglomerate with a dip angle of ~65° at a depth of 46.45 m.

fault with a thrust component in the world (Harris, 2017). The creeping segment extends from surface to a depth of 5 km inferred by seismological observations (Wu et al., 2006). It displays clear seasonal variation of creep rates ranging from ~12 mm/yr in the dry season to ~24 mm/yr in the wet season at the Chinyuan site (Lee et al., 2003). The 2003 Chengkung earthquake did not cause surface rupture along the Chihshang Fault but resulted in a perturbation of the creep rates (i.e., an increase of creeping rates; Lee et al., 2006; Mu et al., 2011). Several boreholes were drilled to intersect the Chihshang Fault (Chen, 2009; Mu et al., 2011), including the WAN-2 borehole that penetrated the Chihshang Fault slip zone. This showed that the Pliocene Lichi Mélange thrusts over Holocene conglomerate (i.e., Holocene alluvial deposits) with a dip of 60–70° (Figure 1c). In contrast to the conglomerates, pervasive shearing occurs within the Lichi Mélange, forming preferentially orientated clasts and widespread scaly clays with slickenside surfaces (Thomas et al., 2014).

In this paper we characterize fault zone materials at a depth of 46.45 m from the WAN-2 borehole. This depth corresponds to the main lithological boundary between the Lichi Mélange and the conglomerate and is considered to be the principal slip zone of the Chihshang Fault and the tectonic plate boundary. Petrographic thin sections were made from the Lichi Mélange, the conglomerate, and the slip zone (corresponding positions are black dashed rectangles in Figure 1c). The borehole was oriented perpendicular to the boundary surface (the red dashed line in Figure 1c). On the basis of the core orientation system (i.e., the lithological boundary dips ~65°), we assume that fault slip was sub-parallel to the dip direction of the boundary (Thomas et al., 2014).

2.2. Field-Emission SEM

A JSM7000F Scanning Electron Microscope (SEM) was used for microstructural study of petrographic thin sections. Energy dispersive X-ray spectroscopy (EDS) and backscattered electron (BSE) imaging were used for semiquantitative measurements of the chemical composition of the analyzed areas and microstructural observations. Thin sections were coated with platinum to increase the electrical conductivity before SEM observations. The SEM was operated at 15-kV acceleration voltage and $2.8 \cdot 10^{-4}$-Pa vacuum, with a 1.5-hr data collection time for X-ray spectrometer elemental mapping.

2.3. FIB-TEM

Analyses using Focused Ion Beam-Transmission Electron Microscope (FIB-TEM) were conducted after the SEM observations. Once the target area was confirmed, the focused ion beam sectioning technique was performed on petrographic thin sections to make ultrathin sections for TEM observations. Ultrathin sections (~200 nm) were retrieved and placed on a copper grid for the TEM observations. It is notable that focused ion beam sectioning techniques may alter the structure of minerals and locally induce amorphization of the sample surface due to the high-energy Gallium-ion beam (Bourdelle et al., 2012). For the phyllosilicates, the thickness of focused ion beam damage is approximately 20 nm in the worst scenario of Bourdelle et al. (2012). Therefore, the original texture of the ultrathin section with a thickness of 200 nm can still be preserved up to 80% from small volume damages by focused ion beam sectioning technique. The instrument for focused ion beam sectioning is a FEI VERSA 3-D at the National Central University, Taiwan, and it is equipped with an electron optics system (high resolution SEM), an ion column optics system (65-nA-current ion column with a gallium ion source), and a gas injection system for platinum deposition. We conducted the TEM experiments with the 200-keV JEM-2000 FXII and the JEM-2100 microscopes at National Central University. We also performed selected area electron diffraction on the ultrathin section with the JEM-2000 FXII, and conducted high-resolution TEM imaging with the JEM-2100 at National Central University. In TEM observation, bright field mode was utilized to show a dark/light contrast between different parts of a structure that are being imaged.

2.4. Monochromatic XRD

We performed X-Ray Diffraction Analysis (XRD) analyses on the bulk rock samples of both the Lichi Mélange and the conglomerate to develop whole (and representative) mineral assemblages, as well as determine the presence of expandable clays. For bulk rock XRD analyses, we pulverized rock samples, disaggregated powders in water, extracted draft suspensions of the clay-sized fraction in the upper part of the container (i.e., ≤ 2 μm based on Stoke's law; Hathway, 1956) and centrifuged and deposited the draft suspensions on glass slides at air-dried or ethylene-glycolated conditions. The Bruker AXS D2 Phaser

X-ray diffractometer in National Central University was used at the conditions of filtered CuKα (1.540 Å) radiation, 30 kV and 10 mA of X-ray generator, 0.6-mm Soller slit, a step of 0.02° with 1.0° min^{-1} scanning speed, and 5–40° of 2θ coverage. We used the commercial software PeakFit 4.12 (Systat Software, Inc., San Jose, CA, USA) to perform peak deconvolution.

Synchrotron XRD analyses were carried out to determine in situ mineral assemblages on the thin sections. Synchrotron XRD analyses were performed at beamline BL01C2 of the National Synchrotron Radiation Research Center in Taiwan. The X-ray wavelength was 0.5166 Å delivered by a double crystal monochromator with two Si(111) crystals and transferred the wavelength of 0.5166 to 1.540 Å (CuKα) for the later data processing (see the supporting information in Kuo, Hsiao, et al., 2014).

2.5. Polychromatic X-Ray Diffraction (Synchrotron Laue Diffraction)

After SEM observations, the analyzed target area on the petrographic thin section was cut into 36-mm^2 pieces (by diamond wire saw; Model STX-202A) and was slightly polished to remove the surface platinum coating for Laue diffraction sample preparation (e.g., Chen et al., 2015; Wenk et al., 1997). Laue diffraction analyses were performed at beamline BL21A of the Taiwan Photon Source in the National Synchrotron Radiation Research Center in Taiwan. Typically, the synchrotron X-ray radiation was generated from two sets of KEKB-type superconducting radiofrequency cavities with a ring energy of 3.0 GeV and a ring current of 500 mA. To provide a scanning-type nanofocusing Laue diffraction technique, the Focusing X-Ray for Microstructural Analysis end station is equipped with an IUT-22 undulator, Si(111) four-bounce channel-cut monochromator, in-vacuum Pilatus3S-6M detector, SEM, and a scanner (SmarAct SLC & SLL positioner). Laue diffraction analysis was conducted with a nanofocused X-ray white beam, Kirkpatrick-Baez mirror, 45° X-ray emission to the sample plane, and acquiring a back-reflection Laue pattern. The high resolution of Laue diffraction in the energy range of ~5–30 keV is achieved with less than 100-nm focused spot size in a high vacuum of 10^{-7} torr. Here, we used the X-ray Microdiffraction Analysis Software (Tamura, 2014) to index Laue diffraction patterns of selected quartz in the slip zone and used MATLAB program developed from National Synchrotron Radiation Research Center to investigate the relative deformation within the quartz grains.

2.6. Permeability and Porosity Measurements

We measured the intrinsic permeability and porosity of the Lichi Mélange and the conglomerate retrieved from the WAN-2 borehole (sampling positions are marked in Figure 6a) with an integrated permeability/porosity measurement system performed at varied isotropic confining pressures and room temperature. Cylindrical samples were prepared in directions perpendicular and parallel to the fault plane to investigate permeability anisotropy. In this study, the confining pressure was increased from 3 MPa to 100 MPa, and then decreased. The permeability was assessed by the steady state flow method (Darcy's law) using helium as the pore fluid. In this method, we gave a steady differential pressure across the sample and then acquire downstream flow rates for the intrinsic permeability determination. The porosity was assessed by the gas expansion method. Given a known pressure in the measurement system with a known volume, the volume of the saturated helium in pore spaces of the sample can be determined from the balanced pressure by using the isothermal gas equations (Dong et al., 2010; Wibberley, 2002). The permeability may be overestimated with respect to the fluid properties because we used gaseous fluids that reach steady state more rapidly than the liquids in natural pore fluids (Tanikawa & Shimamoto, 2006).

3. Microstructural Observations, Microanalytical Results, and Transport Properties

3.1. Microstructural Observations

3.1.1. Optical Microscope Observations

In the footwall of the Chihshang Fault the conglomerate is yellowish brown in color, well lithified, and matrix supported with larger sandstone fragments (approximately centimeters in size). It is also crosscut by a few fractures (Figures 2a–2c). In the matrix of the conglomerate, quartz grains are abundant, especially in sandstone fragments. In contrast, the Lichi Mélange in the hanging wall is characterized by gray, poorly lithified, matrix supported textures with <1 cm mudstone fragments. It contains abundant microfractures

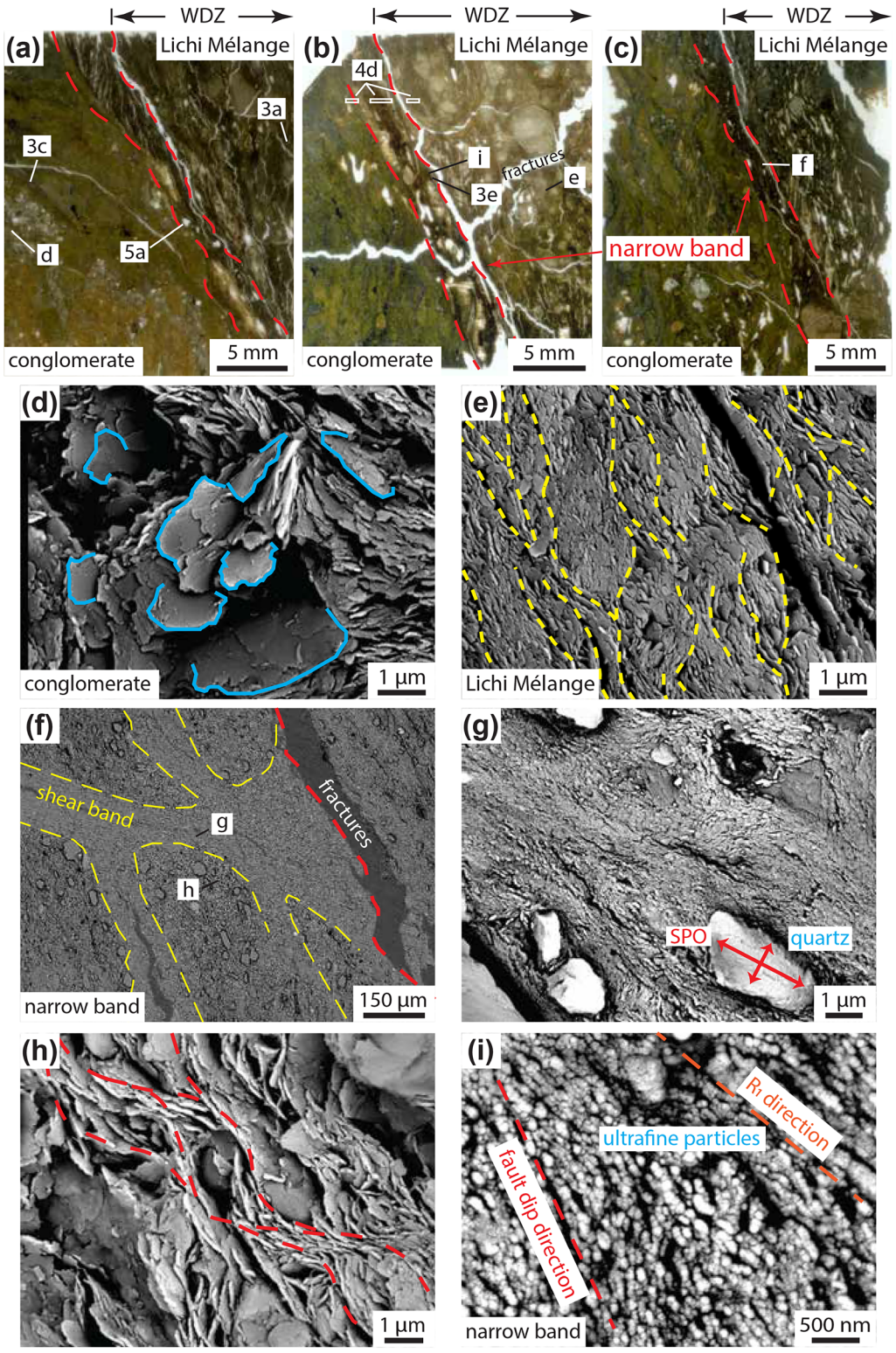

Figure 2. Microstructures of the Lichi Mélange, the conglomerate, and the narrow band from optical and SEM observations. (a–c) An ~3-mm-wide narrow band is recognized at the lithological boundary at which the Lichi Mélange thrusts over the conglomerate. WDZ: wide deformation zone. (d) Clays with euhedral crystal forms and random orientation in the conglomerate. (e) Scaly clays within the Lichi Mélange close to the narrow band. (f) narrow band is recognized as a localized layer with several shear bands. (g) Shear bands show ultrafine clays and particles as a cohesive matrix containing quartz grains with a shape-preferred orientation (SPO). (h) The localized layer (compared to shear band) shows preferential alignment of clays in the matrix and a shape-preferred orientation of quartz. (i) Preferentially oriented ultrafine particles (dozens of nanometers) within the narrow band.

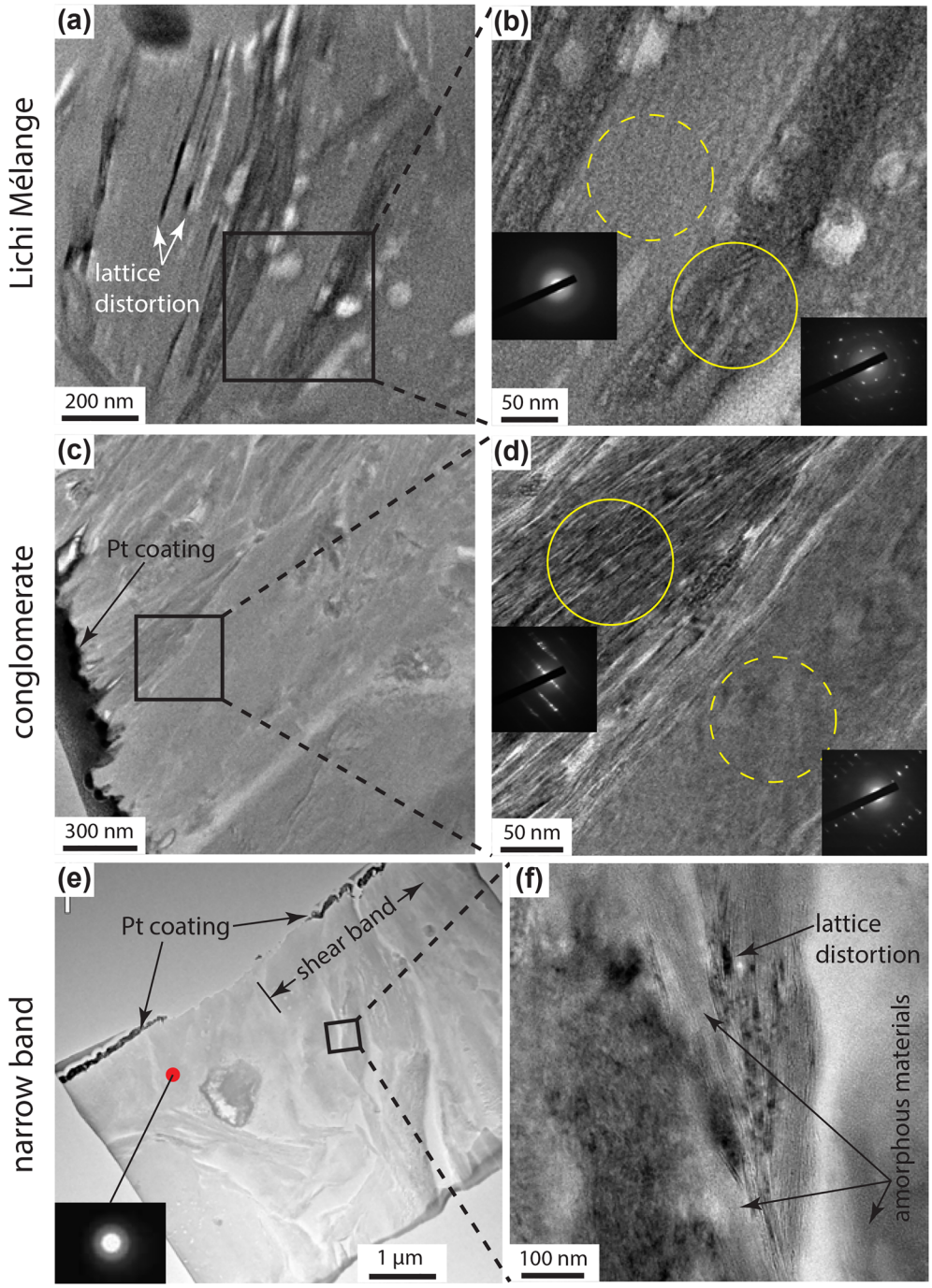

Figure 3. Microstructures of the Lichi Mélange, the conglomerate and the narrow band from TEM observations. (a) Scaly clays show lattice distortions normal to the *c* axis of minerals within the Lichi Mélange. (b) The zone of amorphous material is toward the (001) crystal plane, and along minerals boundaries. Amorphous area is confirmed by SAED. (c) Oriented clays occur in the conglomerate. Pt: Platinum. (d) The zone of crystalline area is similar to the appearance of crystalline and amorphous area in (b) under TEM imaging. (e) Scaly clays and shear band occur in the ultrathin section made by FIB. Amorphous area is recognized by SEAD. (f) Amorphous materials occur towards scaly fabrics.

and a fault-parallel foliation characterized by scaly clay fabrics. An approximately 3-mm-wide discrete dark zone (called localized narrow band hereafter) is recognized at the lithological boundary between the Lichi Mélange and the conglomerate (e.g., Figure 2b).

3.1.2. SEM Observations

Clay minerals in a petrographic thin section are difficult to clearly identify because of their small grain sizes, so we initially observed the microstructures of the clays in our sample with BSE images by SEM. In the matrix of the conglomerate, most of the clays are randomly oriented, euhedral crystal (Figure 2d). In contrast, the Lichi Mélange is characterized by scaly clay fabrics defined by subparallel, anastomosing clay minerals (Figure 2e).

The localized narrow band is a texturally distinct slip layer that lies immediately beneath the Lichi Mélange and is subparallel to the fault slip direction. The localized narrow band generally contains a single dark layer, but in several places is divided by small quartz clasts into several smaller shear bands (Figure 2f). Shear bands are composed of ultrafine clays and particles as a cohesive lump, and the long axes of quartz grains are parallel to sub-parallel to the fault slip direction (Figures 2g and 2i). In addition, the localized narrow band is characterized by a shape preferred orientation of quartz and the preferential alignment of clays in the matrix (Figures 2f and 2h).

3.1.3. Microstructural Observations of FIB-TEM

Bright-field FIB-TEM observations show the microstructures and crystallinity of the observed area in the Lichi Mélange, the conglomerate, and the narrow band. The lattice-fringe image of the Lichi Mélange shows lath-shaped clays and some surrounding particles, likely the relics of quartz grains (Figure 3a). Amorphous textures identified by selected area electron diffraction were observed toward the boundary of scaly clay fabrics, and the lattice distortion was also evident along the scaly clay fabrics that appears as fringe bending and interfering in the darkest areas of the TEM images (Figures 3a and 3b). The interfaces between amorphous and crystalline phases (clays) are atomically sharp, showing a consistent orientation of scaly clay fabrics. In the conglomerate, new growth of clay minerals was observed in some pore spaces. These authigenic grains are irregularly oriented compared with those from the Lichi Mélange (Figure 3c). In contrast to the Lichi Mélange, most of the clay minerals appear defect free, although locally some dislocations can be observed. Due to spacing variation caused by the random interlayering between Illite and I/Ssm, the reciprocal-lattice rods lengthen, thus inducing the streaking of *00l* diffractions (Figure 3d). Within the narrow band, amorphous textures were observed both in the matrix (Figure 3e) and along shear bands, sometimes together with lattice distortions (dark area in Figure 3f).

3.2. Mineral Assemblages

The XRD patterns show the similarity of mineral assemblages between the Lichi Mélange and the conglomerate; both units are composed of chlorite, illite, kaolinite, mixed-layer clays, feldspar, and quartz (Figure 4a). The peak deconvolution of air-dried-subtracted XRD patterns (the area shown in yellow color in Figure 4a) was obtained for the determination of mixed-layer clays (Figures 4b and 4c). Three mixed-layer minerals from the generated peaks are recognized, including an ordered illite/smectite mixed-layer mineral with low smectite content (referred to I/Sil), a poorly crystalline illite/smectite mixed-layer mineral with high smectite content (referred to I/Ssm), and chlorite/vermiculite mixed-layer minerals (referred to Chl/Ve; Figures 4b and 4c).

There is a well-defined sequence of minerals transformations during the illite-to-smectite transition: illite to ordered I/S to disordered I/S to smectite (Hower et al., 1976; Lanson & Champion, 1991; Velde & Vasseur, 1992). In XRD studies, the peak parameters (peak position and full width at half height (FWHM)) of illite and I/S are commonly used to estimate the degree of the weathering process (e.g., Kuo et al., 2012). In the conglomerate, I/Ssm and I/Sil are 11.59 Å (peak position at 7.62° in 2θ) with 1.89°2θ in width (FWHM) and 10.59 Å (peak position at 8.34° in 2θ) with 0.73°2θ in width (FWHM), respectively. In the Lichi Mélange, the peak positions and FWHM of I/Ssm and I/Sil are 12.81 Å with 2.25°2θ in width and 10.88 Å with 1.16°2θ in width, respectively. In summary, compared to the conglomerate, a larger peak width of I/Sil and I/Ssm and relatively smectite-rich I/Ssm (results in higher d spacing of I/Ssm) were obtained in the Lichi Mélange samples. In the discussion section the XRD data will be utilized for clarifying the origin of clay minerals (detrital, weathering, or fault-related processes), which is highly relevant to the interpretation of the formation of AMs.

We conducted synchrotron XRD with a beam diameter of 200 μm and probed the in situ mineral assemblages from the Lichi Mélange (four XRD data), the narrow band (six XRD data), and the matrix of the conglomerate (three XRD data). Because in situ synchrotron XRD penetrates the petrographic

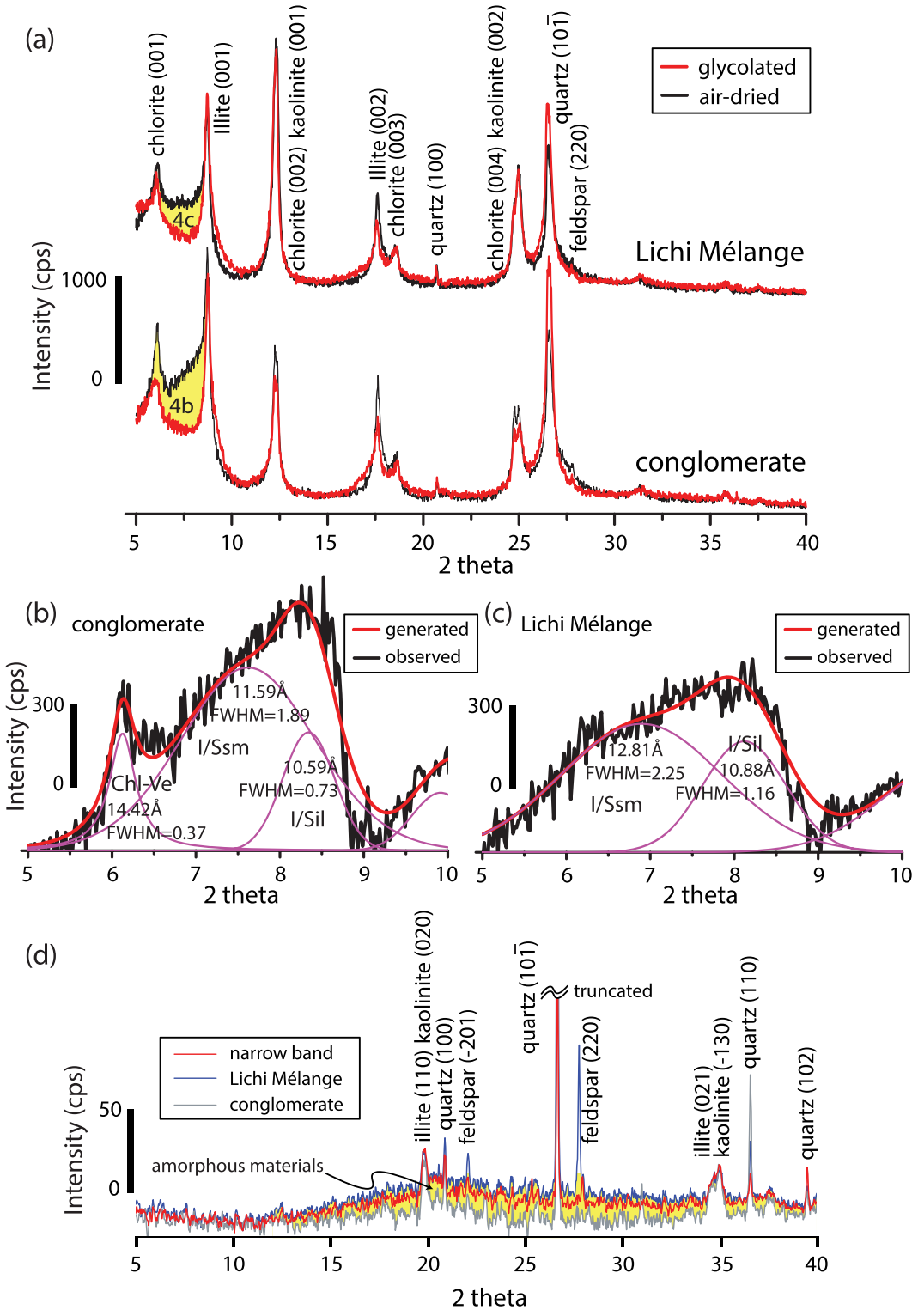

Figure 4. Results of monochromatic diffraction. (a) XRD on the conglomerate and the Lichi Mélange powder sample at air-dried and glycolated conditions. (b) The determination of mixed-layer minerals is obtained from XRD pattern analysis. The group in the conglomerate is composed of Chl/Ve, I/Ssm, and I/Sil. (c) Mixed-layer minerals in the Lichi Mélange are composed of I/Ssm, and I/Sil with different FWHM and peak position. (d) The result of in situ synchrotron XRD. Analyzed points are aligned and across the lithological boundary, and the fractures and large grains were avoided. The occurrence of amorphous materials in the Lichi Mélange and the narrow band is based on the area beneath the XRD curve for the range of 2θ from 15° to 40°.

thin section and collects signal from both materials and glass (thin section), we analyzed a blank area of the thin section and set the obtained XRD patterns as the contribution derived from the thin section. After subtracting the contribution of the thin section (assume that the thickness of the thin section is identical), the representative XRD patterns of the Lichi Mélange, the narrow band, and the matrix of the conglomerate can be determined as the average values of the analyzed areas (Figure 4d; see the detail in Kuo, Hsiao, et al., 2014).

The results of synchrotron XRD show that (1) the Lichi Mélange is composed of illite, kaolinite, quartz, and feldspar; (2) the conglomerate is composed of illite, kaolinite, and quartz; and (3) the narrow band, similar to the Lichi Mélange, is composed of illite, kaolinite, and quartz, but with relatively little feldspar compared with the Lichi Mélange. Because the incident synchrotron X-ray is perpendicular to the *c* axis of preferentially oriented clay on the petrographic thin sections, the strongest diffraction planes (001) and (002) of the clay minerals are low intensities (<14° in 2θ), unlike the XRD data derived from preferred-oriented clay samples. It is interesting that the XRD backgrounds (ranging from 15° to 40° in 2θ) of both the Lichi Mélange and the narrow band are higher than the one of the conglomerate. The difference in the background of XRD patterns (shown the area in yellow in Figure 4d) suggests the presence of AMs in both the Lichi Mélange and the narrow band. This is consistent with the discovery of the presence of AMs from TEM diffraction and high-resolution images.

3.3. Laue Diffraction on Quartz Within the Narrow Band

Several quartz grains can be observed within the narrow band. On the basis of SEM and BSE images with EDS mapping, we selected an ~400-μm quartz grain (largest quartz grains with angular shapes) within the narrow band for better collection of Laue diffraction data (Figures 5a and 5b). Laue diffraction can be utilized to estimate stresses stored in the analyzed mineral by determining its lattice distortions (Chen et al., 2015). Because of the high spatial resolution of Laue diffraction analyses, the imaging is a mosaic and comprises numerous analyzed areas, which are each <100 nm in size. In the analyzed area, the Laue diffraction data contain a set of spots derived from the crystal lattice (Figure 5c). The spots have varied shapes as a result of the different extent of lattice distortion (Figures 5d–5g). The Laue diffraction spots were indexed by software developed by Nobumichi Tamura (see the details in Tamura, 2014). By indexing the spots, we can determine the degree of lattice distortion along the crystal planes in the studied quartz (Figure 5c).

Diffraction peak width of a mineral can be used to determine its crystallinity (e.g., Kuo et al., 2012). To visualize the extent of the crystal lattice of the quartz, we integrated volume mapping of the basal slope of diffraction peaks that can indicate diffraction peak broadening in the quartz. The total peak area, defined by triple full width at half maximum (FWHM), minus the area covered by one FWHM and leaves the area beneath the basal slope (the filled colored areas in the inset of Figure 5h), as representative of crystallinity.

Most of the analyzed grain is crystalline (shown in green and blue colors in Figure 5h) corresponding to undeformed Laue spot patterns (Figure 5(d)). The upper-right portion of the quartz grain shows twisting and elongated Laue spots (Figure 5e), suggesting slight bending of the lattice in this area. On the other hand, severe bending associated with the intense peak broadening was observed in the lower-left portion of the quartz grain, suggesting the presence of significant strain and poor crystallinity. The boundaries between poor and strong crystallinity are indicated by the sharpness of the crystallinity contrast via high spatial resolution of Laue diffraction and were used for the interpretation of kinematic information of fault slip later.

3.4. Permeability and Porosity Data of Rock Samples

We retrieved the WAN-2 cores at depths of 45.40 m (the Lichi Mélange samples) and 46.6 m (the conglomerate samples) for permeability measurements (Figure 6a). The cylinder samples for permeability measurements were made in direction both parallel and perpendicular to the fault plane (i.e., the plane of narrow band). In general, the permeability of the conglomerate is higher than the Lichi Mélange, and it has a higher degree of pressure sensitivity than the Lichi Mélange. Additionally, fault-parallel permeability is higher than fault-perpendicular permeability. It is noteworthy that the fault-parallel permeability of the Lichi Mélange is lower than the fault-perpendicular permeability at 10-MPa confining pressure. The permeability variation

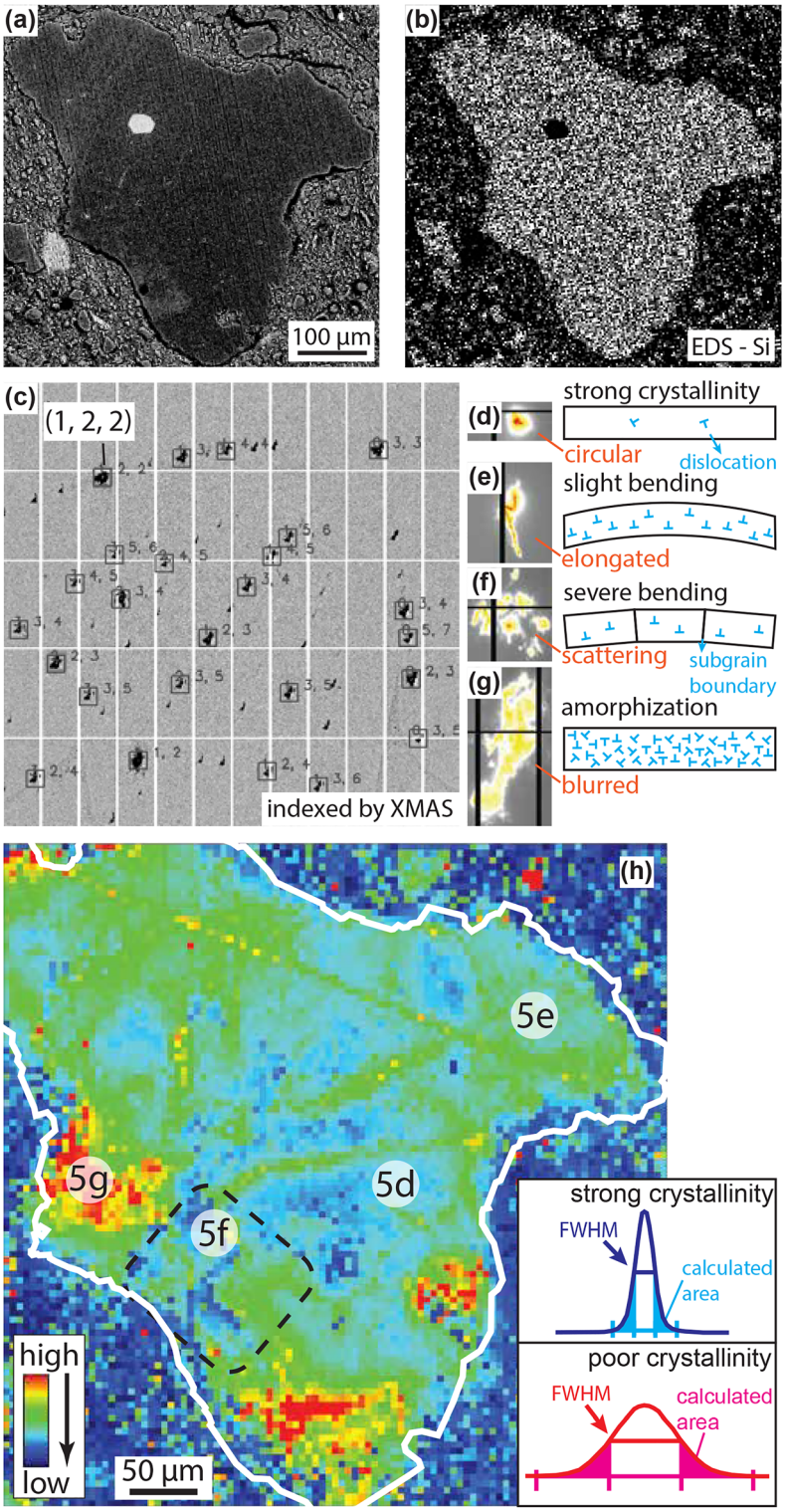

Figure 5. Laue diffraction pattern and mapping on the quartz grain within the narrow band. (a) The analyzed quartz in a SEM image. (b) Mapping of silicon obtained from EDS. (c) One Laue diffraction data show Laue spots with a certain pattern (representing quartz). We can index the Laue pattern by the program XMAS (X-ray Microdiffraction Analysis Software; Tamura, 2014). (d) The circular spot represents the peak of strong crystallinity. (e) The elongated spot with streaked peak represents slight bending and corresponds to geometrically necessary dislocations. (f) The scattering spot with split peaks represents severe bending and corresponds to geometrically necessary boundaries. (g) The blurred spot of peak broadening represents extremely poor crystallinity and corresponds to the defect-rich areas. (h) Integrated volume mapping of the basal slope. Note that the scale bar is relative value. Inset illustrates the calculated area of basal slope.

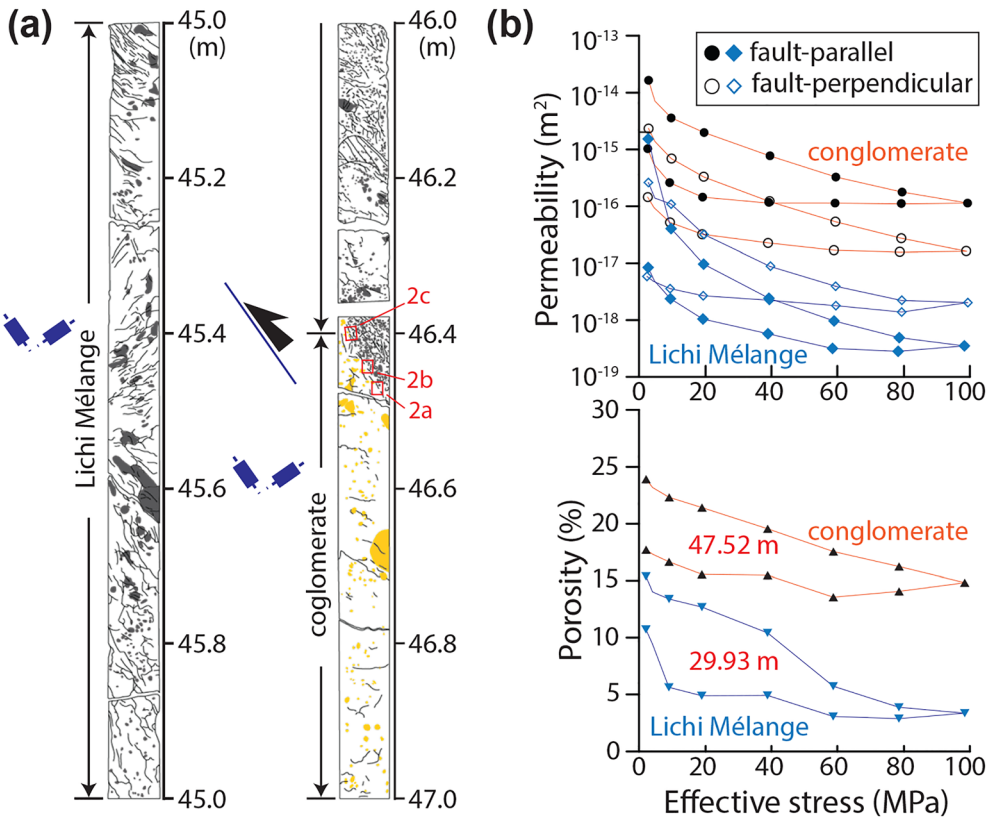

Figure 6. (a) Schematic logs through 2-m-long rock cores and sampling for permeability measurements. Rectangles represent the sampling position with dashed lines meaning measurement directions. (b) Permeability and porosity variations with effective confining pressure. Note that the depths of samples for porosity data is shown (47.52 and 29.93 m).

with confining pressure indicates that (1) the muddy matrix of the Lichi Mélange has low permeability, (2) permeability variation of the Lichi Mélange is significant at low confining pressures (e.g., <30 MPa), and (3) permeability variation of the conglomerate is less sensitive to confining pressure. Our experimental results show that permeability anisotropy exists in the Lichi Mélange and the conglomerate. The Lichi Mélange is likely to be an efficient fluid path in fault-parallel directions in the shallow crust. In addition, the samples for porosity measurements were retrieved from depths of 29.93 and 47.52 m. Experimental results show that the porosity of the conglomerate is higher than that of the Lichi Mélange. In the loading stage, the porosity of the conglomerate ranges from 23.9% at 3 MPa to 14.85% at 100 MPa, whereas the porosity of the Lichi Mélange ranges from 15.4% at 3 MPa to 3.37% at 100 MPa (Figure 6b).

4. Discussion

We discuss the identified clay groups first to evaluate the possibility of weathering for the observed AMs. On the basis of microstructural and mineralogical analysis, we interpret the three clay groups as detrital (Group I chlorite and illite), weathering authigenic (Group II Chl/Ve, Group II I/Ssm, I/Sil, and kaolinite in the conglomerate), and synfaulting authigenic (Group III I/Ssm, I/Sil, and kaolinite in the Lichi Mélange) populations.

Kübler (1964) introduced illite crystallinity as the FWHM of the 10 Å peak, namely, Kübler index (KI), and the unit of illite crystallinity is used to express as °Δ2θ (Dorsey et al., 1988). The glycolation and air-dried X-ray diffraction data of Group I showed that the KI values of Group I were varied from ~0.3 to ~0.5 in °Δ2θ, which is consistent with the common group of clay minerals (as detrital phases) in sedimentary rocks in Taiwan (Kuo et al., 2012). Group I in both the conglomerate and the Lichi Mélange, therefore, can be

considered to be detrital (Haines & van der Pluijm, 2012; Kuo et al., 2012). We discuss Group II (in the conglomerate) and Group III (in the Lichi Mélange) in detail below and interpret the mechanisms responsible for the observed AMs.

4.1. Weathering Authigenic Population in the Conglomerate

Clay minerals in faulted sedimentary rocks can form due to mechanical incorporation from host rocks into the fault zone (Jones & Hillis, 2003; Yielding et al., 1997), or from chemical reactions that occur during weathering and tectonic fluid–rock interactions over long periods of time (Solum et al., 2005; Vrolijk & van der Pluijm, 1999). Distinguishing the dominant factors (fluid activity and composition, temperature, strain, and time) that control clay genesis and clay transformation (e.g., illite-smectite transformation) within fault zones remains challenging (e.g., Essene & Peacor, 1995; Kuo et al., 2011; Moore & Reynolds, 1997; Solum et al., 2005). Four lines of evidence suggest that the Group II clays in the conglomerates were mainly derived from weathering processes: (1) textures suggesting fault-related deformation (Figures 1c and 2d) are lacking, implying the clays might be formed by weathering rather than by faulting; (2) the conglomerate has high porosity and permeability (Figure 6), which would allow penetration of meteoric fluids and is capable of forming new hydrated species; (3) the absence of K-feldspar (Figure 4d) and the presence of both kaolinite and illite suggest the alteration of K-feldspar (K-feldspar→illite+kaolinite, or K-feldspar→(illite) + smectite+kaolinite; Beaufort, 1987); (4) the morphology (hexagonal lamella) of illite and its grain size (Figure 2d) suggests the growth of clay in porous conditions (the evolution of illite tends toward isometric shapes as the size increase; Lanson & Meunier, 1995). Therefore, the mineral assemblages and microstructural observations documented here in Group II (I/Ssm, I/Sil, Chl/Ve, and kaolinite) are interpreted to have formed by weathering and alteration of Group I minerals (chlorite, illite, and feldspar).

Weathering processes can result in the generation of AMs as a thin film on the surface of the weathered materials. For example, amorphous thin layers have been generated by in situ hydration of the crystalline matrix in quartz (Pope, 1995); chemical leaching and reprecipitation of a detached silica layer (Hellmann et al., 2003); repolymerization and condensation of a layer (Casey et al., 1993); and on a naturally weathered surface on feldspar (Zhu et al., 2006). The aforementioned amorphous thin layers commonly appeared at the rim of those minerals with an average thickness of ~50 nm. The FIB-TEM results of the conglomerate from the (limited) studied area demonstrate the absence of AMs, diminishing the possibility of fluid-induced amorphization in the conglomerate in which the weathering process took place during the long-term geological time.

4.2. Synfaulting Authigenic Population in the Lichi Mélange

Weathering-related authigenic processes seem to occur in the Lichi Mélange because of the presence of I/Ssm (Group III) that was derived from the alteration of Group I minerals (Figure 4c). However, we argue that weathering-related authigenic processes are not fully responsible for the formation of I/Ssm (Group III) for two reasons: (1) the permeability data (in the static state) show that fluid flow within the Lichi Mélange is probably slower than in the conglomerate, both in fault-parallel and fault-perpendicular directions (Figure 6b). This suggests that weathering (fluid–rock interaction) triggered by the penetration of meteoric fluids should be diminished in the Lichi Mélange (compared to the conglomerate); (2) shearing in the mudstone can reduce the fault-perpendicular permeability and result in undrained behavior during slip (Ikari & Saffer, 2012). The reduction of shearing-induced permeability (in the dynamic state) would impede fluid transportation within the deformed materials, suggesting the development of an unfavorable environment for weathering processes.

Compared to the conglomerate, the Lichi Mélange samples contain a larger peak width of I/Sil and I/Ssm and relatively smectite-rich I/Ssm. This shows that both I/Sil and I/Ssm is relatively poorly crystallized (disordered), and the extra smectite content in the I/Ssm (Merriman & Peacor, 1999). Integrated with the discussion that weathering processes were inefficient within the Lichi Mélange, this strongly suggests the presence of an additional mechanism involved for Group III minerals (poor crystallinity of I/S and an increase of smectite interlayers in I/S) in the Lichi Mélange. Most importantly, Group III is deformed and occurs in shear zones. The difference in crystallinity between group II and group III indicates that relatively high disorder in Group III is presumably due to shearing and weathering of Group I (chlorite and illite). Therefore,

we suggest that the poor crystallinity of Group III is the response to an increase of the number of defects caused by stress and intense deformation to cause single crystals to be divided into subgrains, or by neoformation of smaller crystals, which is in good agreement with the microstructural observations (Figures 2e–2g). It is notable that strain can broaden the peaks of clays, and further Rietveld methods on random powder diffraction profile may be required to evaluate the strain broadening of the peaks of clay minerals in the future (e.g., Ufer et al., 2012).

4.3. Shear-Induced Amorphization in the Lichi Mélange

Because Group III minerals were formed by relatively less fluid circulation compared to that in the conglomerate and showed defect-dominated crystallinity within shear zones, we suggest that mechanical processes, particularly the comminution process (Janssen et al., 2010; Ozawa & Takizawa, 2007; Pec et al., 2012, 2016; Yund et al., 1990), is the dominant driving process for the generation of AMs in the Lichi Mélange (AMs were not observed in weathering-dominated conglomerate; Figure 4). AMs were observed both on the interface of scaly clay fabrics and within the localized narrow band (Figures 3 and 4), and therefore, we discuss the occurrence of these types of AMs separately based on the mechanical origin mechanism.

Scaly clay fabrics can form through more than one mechanism in nature, but during deformation the slip behavior is suggested to be similar (slip occur along scaly clay fabrics' shear surfaces) once the geometry has been established (Haines et al., 2013; Tarling & Rowe, 2016). AMs were observed at the contact of the boundaries of scaly clay fabrics (Figures 3a and 3b), suggesting that slip occurred along the shear surfaces of the scaly clay fabrics during deformation. However, both incremental slip on individual wavy shear surfaces, and multiple shear surfaces across an anastomosing network deforming simultaneously, could result in the production of AMs, and we cannot constrain the slip styles in our case.

Ultrafine particles and AMs coexist within the narrow band (Figure 2i, 3e, and 3f). Ultrafine particles have been found in a wide range of faulted rock types within natural faults (Chester et al., 2005; Kirkpatrick et al., 2013; Ma et al., 2006; Ozawa & Takizawa, 2007), in particular, in the principal slip zones that accommodate the bulk of displacement during faulting (PSZs; Sibson, 2003). In addition, because strain is highly localized during friction experiments, ultrafine particles were experimentally formed in a thin PSZ (~a few hundred micrometers to few millimeters in thickness) in a wide range of conditions (seismic to aseismic rates with the upper-crustal loading) and were frequently found in association with partially amorphized materials (Aretusini et al., 2017; Pec et al., 2016). Since the narrow band was found in the Lichi mélange and at the lithological contacts (Bullock et al., 2014; Fagereng & Sibson, 2010; Figure 1), we interpret that the narrow band was derived from strain localization and represents the PSZ of the Lichi Mélange.

The Laue diffraction spots, showing low-intensity, broadened peaks and difficulty of indexing, illustrate an extremely poorly crystallized zone of quartz (Figure 5h) and directly indicate the presence of an amorphous phase. Deformation lamellae are considered as the sites for the nucleation of amorphous phases (Kingma et al., 1993). The crystal lattices within quartz show deformation lamellae (Figures 5h and 7) that are coincidently subparallel to the assumed fault slip direction. Neither the preexisting defects nor the obliteration and regeneration of deformation lamellae (over a long-term geological time) were observed in the quartz grain. This implies that the quartz grain was dragged rather than rotated within the narrow band and locally preserves kinematic information related to fault slip. In addition, the crystalline-to-amorphous phase transition has been observed over a broad range of pressure (i.e., at 1–4 GPa) and shear stress in comminution, static compression and shock compression experiments (i.e., up to 40 GPa) (Kingma et al., 1993). Considering the depth of borehole cores in this study, the lithostatic pressure is much lower than that obtained in the high-pressure experiments, and other stresses are required for the crystalline-to-amorphous phase transition, for example, localized shear stress. The amorphous phase may be as a result of stress concentration within cohesive narrow band, where the cohesion achieves the stress transmission which is probably like the occurrence of force chains.

Different from commonly reported shear-induced crystallization on fault rocks (e.g., shear-induced graphitization; Kuo, Li, et al., 2014, 2017), shear-induced amorphization (not pseuotachylyte that as the case of frictional melting and quickly quenched) has also been reported in different settings: A localized amorphous band can be formed by dislocation glide in metal alloys, along the shear direction or primitive grain

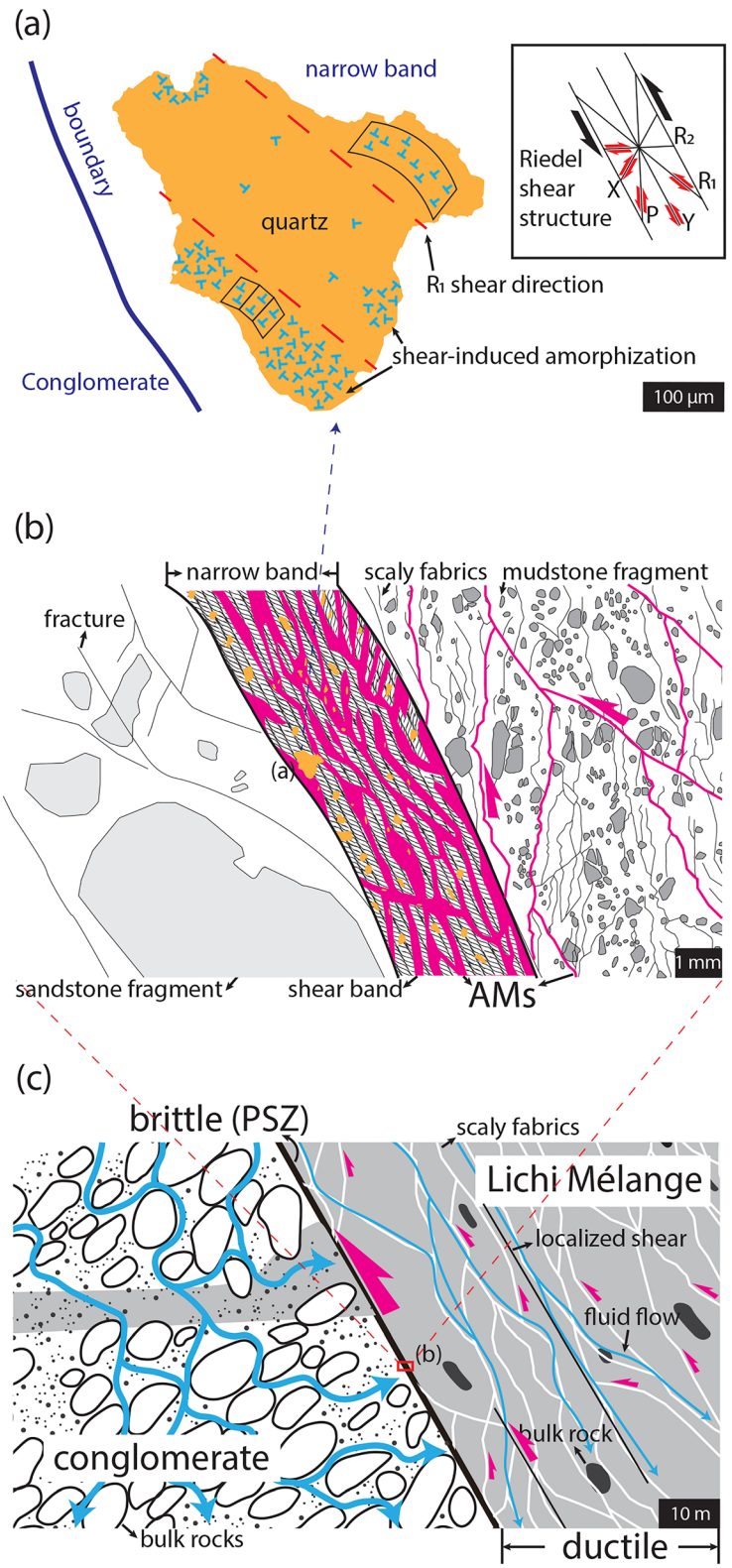

Figure 7. Schematic diagram shows the concept of strain dissipation in the Chihshang Fault and the Lichi Mélange based on microstructural observations. (a) Shear-induced amorphization and lattice deformation occur in quartz grain, bounded by the R_1 shear direction. (b) Amorphous materials occur in a narrow band (localized in shear band) and along the interface of scaly clays in the Lichi Mélange. (c) Amorphization is driven by tectonic loading and reflects a mixed brittle and ductile deformation style in the Chihshang Fault.

boundary (Peterlechner et al., 2009); shear-driven amorphization occurs within a shear band and then proceeds by deformation-induced dislocation nucleation and accumulation on silicon crystals (He et al., 2016; Zhao et al., 2016); in experiments conducted under midcrustal conditions, amorphous bands formed in slip zones consisting of (partial) AMs (Pec et al., 2012, 2016). Taken together, the synchrotron Laue diffraction has demonstrated the presence of amorphized areas in the quartz grain, suggesting strain localization and associated shear-induced amorphization within the narrow band.

4.4. Implications of Mixed Deformation Styles in the Chihshang Fault

Direct information about the deformation styles of the analyzed fault rocks (i.e., strain in bulk) cannot be obtained from our data. However, we do find shear-induced amorphization and the associated AMs in both the localized narrow band (PSZ) and along the boundaries of widely distributed scaly clay fabrics (with limited sample observations), likely marking the distribution of dissipated strain in the Lichi Mélange. Natural and experimentally formed PSZs are commonly treated as frictional interfaces embedded in host rocks, suggesting brittle behavior in the bulk fault rocks (Ikari, 2015; Sibson, 2003; Verberne et al., 2019). On the other hand, small amounts of slip occurring along the boundaries of abundant scaly clays allow the fault rock to deform with a ductile behavior. Therefore, the occurrence of AMs in the Lichi Mélange may be related to both brittle and ductile deformation styles in fault rocks during tectonic loading and stress relaxation. The deformation styles in the Lichi Mélange can be compared with other mélanges. Deformation in mélanges (i.e., competent domains vs. incompetent domains) is mainly accommodated by viscous strain on multiple slip surfaces and results in heterogeneous continuous-discontinuous shear zones (Fagereng & Sibson, 2010). The coexistence of pseudotachylyte and mylonite has shown that mixed seismic-aseismic deformation styles can coexist in mélange shear zones and that ductile mylonitic rocks can experience brittle rapid earthquake deformation during the seismic cycle (Chu et al., 2012; Passchier, 1982; Ueda et al., 2008).

Based on our results, we propose a possible model for the creeping fault zone of the Chihshang Fault, shown in the schematic diagram of Figure 7. Laue diffraction data (Figure 5) show that two (almost) parallel boundaries divide the quartz grain into three crystal domains that are disordered, undeformed, and highly disordered (Figure 7a). These crystallinity boundaries intersect obliquely (<20°) with the edges of the narrow band and main lithological boundary between the conglomerate and the Lichi melange. Because the localized narrow band is simply treated as a frictional interface embedded between the conglomerate and the Lichi Mélange, the crystallinity boundaries of the analyzed quartz grain derived from shear-induced amorphization may possibly provide kinematic information related to fault slip. Within the narrow band, the geometry of the crystallinity boundaries of the analyzed quartz grain and ultrafine particles are consistent with the orientation of R_1 shears, while the narrow band represents the *Y* shear orientation. (Ikari et al., 2011; Loagn et al., 1992; Rutter et al., 1986; Figure 7a, inset).

Considering the distribution of AMs and likely the dissipation of strain, we suggest that fault slip occurs within the localized narrow band and along the boundaries of scaly clays (Figure 7b). Rather than the localized strain within the discrete narrow band, scaly clay fabrics may allow distributed shear deformation within anastomosing networks of slip surfaces, resulting in bulk ductile flow (Tarling & Rowe, 2016). Therefore, we propose that the creeping zone of the Chihshang Fault was by both brittle and ductile deformation styles to produce AMs within the narrow band and along scaly clay fabrics (Figure 7c).

On the other hand, weathering and fluid-rock interaction (mineralization) processes occur in the relatively porous conglomerate (and to a lesser extent within the Lichi Mélange) where fluids are able to circulate along grain interfaces and deposit hydrated clay phases (Group II and III). We cannot constrain the water chemistry in the area and simply assume that the formation of I/S and Chl/Ve originated from the interaction of K^+-rich fluids (Offler & Prendergast, 1985), sourced by the dissolution of K-feldspars present in the host rocks. In addition, we do not have direct evidence of glass-smectite transformation (e.g., Janssen et al., 2014), but the observed increase of I/Ssm (Group III) could be important for the behavior of the Chihshang Fault. An increase of smectite phases in I/S interstratified clays within slipping fault zones and fractures (between scaly clay fabrics) was proposed as a mechanism for reducing fault strength, facilitated creep and enhancing the potential for fault reactivation (e.g., Haines & van der Pluijm, 2012; Morrow et al., 2017). Therefore, we propose that the formation of AMs by shear-induced amorphization can be likely considered as precursors for the formation of I/Ssm (Bettermann & Liebau, 1975; Tomita et al., 1993), and

the transformation of fault-zone materials by gouge amorphization could potentially modify the mechanical, physical, and chemical properties of the fault zone and promote the currently observed creeping behavior at shallow depths.

5. Conclusions

We demonstrate the presence of AMs in the actively creeping Chihshang Fault in Taiwan and suggest that the AMs were derived from shear-induced amorphization process. In addition, we interpret the occurrence of AMs in two structural locations (a localized narrow shear band and within distributed networks of scaly clay fabrics) as a likely consequence of the dissipation of strain during mixed brittle to ductile deformation. Because AMs are kinetically unstable in low-temperature environments at depth, their presence within the Chihshang Fault suggests recent and ongoing on-fault amorphization driven by tectonic loading and stress relaxation. Integrated with data on the populations of phyllosilicates within the creeping fault zone (in particular, an increase of smectite content in I/S mineral; Group III), we propose that shear-induced amorphization gradually modifies the physical, chemical, and mineralogical characteristics of a fault by amorphous phase and subsequent neomineralization. Minerals in a fault zone may be altered so the properties of fault gouge such as the friction and chemical composition might change. Shear-induced amorphization likely serves as a mechanism that influences the dynamic fault strength and seismogenesis at shallow depths during the seismic cycle.

Data Availability Statement

All the experimental raw data are available in figshare with the identifier (https://doi.org/10.6084/m9.figshare.12269486.v1).

Acknowledgments

This research used materials provided by the Central Geological Survey, Taiwan. It was supported by the Taiwan ROC (Republic of China) Ministry of Science and Technology (MOST 108-2116-M-008-021-MY2) and Earthquake-Disaster & Risk Evaluation and Management Center, E-DREaM" from The Featured Areas Research Center Program within the framework of the Higher Education Sprout Project by the Ministry of Education (MOE) in Taiwan to Li-Wei Kuo. Samples were prepared by Dr. Jialiang Si via the National Science Foundation of China (41872211). We sincerely thank Dr. Dennis Brown and Dr. Steven A.F. Smith for reorganizing and polishing the manuscript. Thanks to Hsiu-Ching Hsiao and Chih-Chuan Huang for their technical support of SEM and TEM at National Central University.

References

Angelier, J., Chu, H.-T., Lee, J.-C., & Hu, J.-C. (2000). Active faulting and earthquake hazard: The case study of the Chihshang Fault, Taiwan. *Journal of Geodynamics*, *29*(3-5), 151–185. https://doi.org/10.1016/S0264-3707(99)00045-9

Aretusini, S., Mittempergher, S., Plümper, O., Spagnuolo, E., Gualtieri, A. F., & Di Toro, G. (2017). Production of nanoparticles during experimental deformation of smectite and implications for seismic slip. *Earth and Planetary Science Letters*, *463*, 221–231. https://doi.org/10.1016/j.epsl.2017.01.048

Beaufort, D. (1987). Interstratified chlorite/smectite ("metamorphic vermiculite") in the upper Precambrian greywackes of Rouez, Sarthe, France. In L. G. Schultz, H. van Olphen, & F. A. Mumpton (Eds.), *Proceedings of the international clay conference* (pp. 59–65). Bloomington, IN: The Clay Minerals Society.

Bettermann, P., & Liebau, F. (1975). The transformation of amorphous silica to crystalline silica under hydrothermal conditions. *Contributions to Mineralogy and Petrology*, *53*(1), 25–36. https://doi.org/10.1007/BF00402452

Bourdelle, F., Parra, T., Beyssac, O., Chopin, C., & Moreau, F. (2012). Ultrathin section preparation of phyllosilicates by focused ion beam milling for quantitative analysis by TEM-EDX. *Applied Clay Science*, *59-60*, 121–130. https://doi.org/10.1016/j.clay.2012.02.010

Bullock, R. J., De Paola, N., Holdsworth, R. E., & Trabucho-Alexandre, J. (2014). Lithological controls on the deformation mechanisms operating within carbonate-hosted faults during the seismic cycle. *Journal of Structural Geology*, *58*, 22–42. https://doi.org/10.1016/j.jsg.2013.10.008

Casey, W. H., Westrich, H. R., Banfield, J. F., Ferruzzi, G., & Arnold, G. W. (1993). Leaching and reconstruction at the surfaces of dissolving chain-silicate minerals. *Nature*, *366*(6452), 253–256. https://doi.org/10.1038/366253a0

Chen, K., Kunz, M., Tamura, N., & Wenk, H.-R. (2015). Residual stress preserved in quartz from the San Andreas Fault Observatory at Depth. *Geology*, *43*(3), 219–222. https://doi.org/10.1130/G36443.1

Chen, W.-S. (2009). The fault slip long term velocity and recurrence period, Report of Central Geological Survey, 31–40.

Chester, J. S., Chester, F. M., & Kronenberg, A. K. (2005). Fracture surface energy of the punchbowl Fault, San Andreas system. *Nature*, *437*(7055), 133–136. https://doi.org/10.1038/nature03942

Chu, H.-T., Hwang, S.-L., Shen, P., & Yui, T.-F. (2012). Pseudotachylyte in the Tananao metamorphic complex, Taiwan: Occurrence and dynamic phase changes of fossil earthquakes. *Tectonophysics*, *581*, 62–75. https://doi.org/10.1016/j.tecto.2012.01.017

Delle Piane, C., Piazolo, S., Timms, N. E., Luzin, V., Saunders, M., Bourdet, J., et al. (2018). Generation of amorphous carbon and crystallographic texture during low-temperature subseismic slip in calcite fault gouge. *Geology*, *46*(2), 163–166. https://doi.org/10.1130/G39584.1

Di Toro, G., Hirose, T., Nielsen, S., Pennacchioni, G., & Shimamoto, T. (2006). Natural and experimental evidence of melt lubrication of faults during earthquakes. *Science*, *311*(5761), 647–649. https://doi.org/10.1126/science.1121012

Dong, J.-J., Hsu, J.-Y., Wu, W.-J., Shimamoto, T., Hung, J.-H., Yeh, E.-C., et al. (2010). Stress-dependence of permeability and porosity of sandstone and shale from TCDP Hole-A. *International Journal of Rock Mechanics and Mining Sciences*, *47*(7), 1141–1157. https://doi.org/10.1016/j.ijrmms.2010.06.019

Dorsey, R. J., Buchovecky, E. J., & Lundberg, N. (1988). Clay mineralogy of Pliocene–Plistocene mudstones, eastern Taiwan: Combined effects of burial diagenesis and provenance unroofing. *Geology*, *16*(10), 944–947. https://doi.org/10.1130/0091-7613(1988)016<0944:CMOPPM>2.3.CO;2

Essene, E. J., & Peacor, D. R. (1995). Clay mineral thermometry—A critical perspective. *Clays and Clay Minerals*, *43*(5), 540–553. https://doi.org/10.1346/CCMN.1995.0430504

Fagereng, A., & Sibson, R. H. (2010). Mélange rheology and seismic style. *Geology*, *38*(8), 751–754. http://doi.org/10.1130/G30868.1

Haines, S. H., Kaproth, B., Marone, C., Saffer, D., & van der Pluijm, B. (2013). Shear zones in clay-rich fault gouge: A laboratory study of fabric development and evolution. *Journal of Structural Geology*, *51*, 206–225. https://doi.org/10.1016/j.jsg.2013.01.002

Haines, S. H., & van der Pluijm, B. A. (2012). Patterns of mineral transformations in clay gouge, with examples from low-angle normal fault rocks in the western USA. *Journal of Structural Geology*, *43*, 2–32. http://doi.org/10.1016/j.jsg.2012.05.004

Harris, R. A. (2017). Large earthquakes and creeping faults. *Reviews of Geophysics*, *55*, 169–198. https://doi.org/10.1002/2016RG000539

Hathway, J. C. (1956). Procedure for clay mineral analyses used in the sedimentary petrology laboratory of the U.S. Geological Survey. *Clay Minerals Bulletin*, *3*(15), 8–13. https://doi.org/10.1180/claymin.1956.003.15.05

He, Y., Zhong, L., Fan, F., Wang, C., Zhu, T., & Mao, S. X. (2016). In situ observation of shear-driven amorphization in silicon crystals. *Nature Nanotechnology*, *11*(10), 866–871. https://doi.org/10.1038/nnano.2016.166

Heaton, T. H. (1990). Evidence for and implications of self-healing pulses of slip in earthquake rupture. *Physics of the Earth and Planetary Interiors*, *64*(1), 1–20. https://doi.org/10.1016/0031-9201(90)90002-F

Hellmann, R., Penisson, J.-M., Hervig, R. L., Thomassin, J.-H., & Abrioux, M.-F. (2003). An EFTEM/HRTEM high-resolution study of the near surface of labradorite feldspar altered at acid pH: Evidence for interfacial dissolution-reprecipitation. *Physics and Chemistry of Minerals*, *30*(4), 192–197. https://doi.org/10.1007/s00269-003-0308-4

Hellmann, R., Wirth, R., Daval, D., Barnes, J.-P., Penisson, J.-M., Tisserand, D., et al. (2012). Unifying natural and laboratory chemical weathering with interfacial dissolution-reprecipitation: A study based on the nanometer-scale chemistry of fluid-silicate interfaces. *Chemical Geology*, *294-295*, 203–216. https://doi.org/10.1016/j.chemgeo.2011.12.002

Hower, J., Eslinger, E. V., Hower, M. E., & Perry, E. A. (1976). Mechanism of burial metamorphism of argillaceous sediment: 1. Mineralogical and chemical evidence. *Geological Society of America Bulletin*, *87*(5), 725–737. https://doi.org/10.1130/0016-7606(1976)87<725:MOBMOA>2.0.CO;2

Ikari, M. J. (2015). Principal slip zones: Precursors but not recorders of earthquake slip. *Geology*, *43*(11), 955–958. https://doi.org/10.1130/G37028.1

Ikari, M. J., & Kopf, A. J. (2017). Seismic potential of weak, near-surface faults revealed at plate tectonic slip rates. *Science Advances*, *3*(11), e1701269. http://doi.org/10.1126/sciadv.1701269

Ikari, M. J., Niemeijer, A. R., & Marone, C. (2011). The role of fault zone fabric and lithification state on frictional strength, constitutive behavior, and deformation microstructure. *Journal of Geophysical Research*, *116*, B08404. https://doi.org/10.1029/2011JB008264

Ikari, M. J., & Saffer, D. M. (2012). Permeability contrasts between sheared and normally consolidated sediments in the Nankai accretionary prism. *Marine Geology*, *295-298*, 1–13. https://doi.org/10.1016/j.margeo.2011.11.006

Janssen, C., Wirth, R., Rybacki, E., Naumann, R., Kemnitz, H., & Wenk, H.-R. (2010). Amorphous material in SAFOD core samples (San Andreas Fault): Evidence for crush-origin pseudotachylytes? *Geophysical Research Letters*, *37*, L01303. https://doi.org/10.1029/2009GL040993

Janssen, C., Wirth, R., Wenk, H.-R., Morales, L., Naumann, R., Kienast, M., et al. (2014). Faulting processes in active faults—Evidences from TCDP and SAFOD drill core samples. *Journal of Structural Geology*, *65*, 100–116. https://doi.org/10.1016/j.jsg.2014.04.004

Jones, R. M., & Hillis, R. R. (2003). An integrated, quantitative approach to assessing fault-seal risk. *AAPG Bulletin*, *87*(3), 507–524. https://doi.org/10.1306/10100201135

Kawano, M., & Tomita, K. (1996). Amorphous aluminum hydroxide formed at the earliest weathering stages of K-feldspar. *Clays and Clay Minerals*, *44*(5), 672–676. https://doi.org/10.1346/ccmn.1996.0440510

Kingma, K. J., Meade, C., Hemley, R. J., Mao, H.-K., & Veblen, D. R. (1993). Microstructural observations of α-quartz amorphization. *Nature*, *259*(5095), 666–669. https://doi.org/10.1126/science.259.5095.666

Kirkpatrick, J. D., Rowe, C. D., White, J. C., & Brodsky, E. E. (2013). Silica gel formation during fault slip: Evidence from the rock record. *Geology*, *41*(9), 1015–1018. https://doi.org/10.1130/G34483.1

Kübler, B. (1964). Les argiles, indecateurs de métamorphisme. *Revue de L'Institut Francais du Petrole*, *19*, 1093–1112.

Kuo, L.-W., Di Felice, F., Spagnuolo, E., Di Toro, G., Song, S.-R., Aretusini, S., et al. (2017). Fault gouge graphitization as evidence of past seismic slip. *Geology*, *45*(11), 979–982. https://doi.org/10.1130/G39295.1

Kuo, L.-W., Hsiao, H.-C., Song, S.-R., Sheu, H.-S., & Suppe, J. (2014). Coseismic thickness of principal slip zone from the Taiwan Chelungpu fault Drilling Project-A (TCDP-A) and correlated fracture energy. *Tectonophysics*, *619-620*, 29–35. http://doi.org/10.1016/j.tecto.2013.07.006

Kuo, L.-W., Li, H., Smith, S., Di Toro, G., Suppe, J., Song, S. R., et al. (2014). Gouge graphitization and dynamic fault weakening during the 2008 Mw 7.9 Wenchuan earthquake. *Geology*, *42*(1), 47–50. https://doi.org/10.1130/G34862.1

Kuo, L.-W., Song, S.-R., Huang, L., Yeh, E.-C., & Chen, H.-F. (2011). Temperature estimates of coseismic heating in clay-rich fault gouges, the Chelungpu fault zones, Taiwan. *Tectonophysics*, *502*(3-4), 315–31.327. https://doi.org/10.1016/j.tecto.2011.02.001

Kuo, L. W., Song, S. R., Suppe, J., & Yeh, E. C. (2016). Fault mirrors in seismically active fault zones: A fossil of small earthquakes at shallow depths. *Geophysical Research Letters*, *43*, 1950–1959. https://doi.org/10.1002/2015GL066882

Kuo, L.-W., Song, S.-R., Yeh, E.-C., & Chen, H.-F. (2009). Clay mineral anomalies in the fault zone of the Chelungpu Fault, Taiwan, and their implication. *Geophysical Research Letters*, *36*, L18306. https://doi.org/10.1029/2009GL039269

Kuo, L.-W., Song, S.-R., Yeh, E.-C., Chen, H.-F., & Si, J. (2012). Clay mineralogy and geochemistry investigations in the host rocks of the Chelungpu fault, Taiwan: Implication for faulting mechanism. *Journal of Asian Earth Sciences*, *59*, 208–218. https://doi.org/10.1016/j.jseaes.2012.07.009

Lanson, B., & Champion, D. (1991). The I/S-to-Illite reaction in the late stage diagenesis. *American Journal of Science*, *291*(5), 473–506. https://doi.org/10.2475/ajs.291.5.473

Lanson, B., & Meunier, A. (1995). La transformation des interstratifiés ordonnés (S≥1) illite-smectite en illite dans les séries diagénétiques: Etat des connaissances et perspective. *Bulletin des Centres de Recherches Exploration-Production Elf-Aquitaine*, *19*, 149–165.

Lee, J.-C., Angelier, J., Chu, H.-T., Hu, J.-C., Jeng, F.-S., & Rau, R.-J. (2003). Active fault creep variations at Chihshang, Taiwan, revealed by creep meter monitoring, 1998–2001. *Journal of Geophysical Research*, *108*(B11), 2528. https://doi.org/10.1029/2003JB002394

Lee, J.-C., Chu, H.-T., Angelier, J., Hu, J.-C., Chen, H.-Y., & Yu, S.-B. (2006). Quantitative analysis of surface coseismic faulting and postseismic creep accompanying the 2003, Mw=6.5, Chengkung earthquake in eastern Taiwan. *Journal of Geophysical Research*, *111*, B02405. http://doi.org/10.1029/2005JB003612

Loagn, J. M., Dengo, C. A., Higgs, N. G., & Wang, Z. Z. (1992). Fabric of experimental fault zones: Their development and relationship to mechanical behavior. *International Geophysics*, *51*, 33–67. https://doi.org/10.1016/S0074-6142(08)62814-4

Ma, K.-F., Tanaka, H., Song, S.-R., Wang, C.-Y., Hung, J.-H., Tsai, Y.-B., et al. (2006). Slip zone and energetics of a large earthquake from the Taiwan Chelungpu-fault Drilling Project. *Nature*, *444*(7118), 473–476. https://doi.org/10.1038/nature05253

Merriman, R. J., & Peacor, D. R. (1999). Low grade metapelites: Mineralogy, microtextures and measuring reaction progress. In M. Frey, & D. Robinson (Eds.), *Low grade metamorphism*, (pp. 10–60). Oxford: Blackwell Science.

Moore, D. M., & Reynolds, R. C. (1997). *X-ray diffraction and the identification and analysis of clay minerals*. Oxford, United Kingdom: Oxford University Press.

Morrow, C. A., Moore, D. E., & Lockner, D. A. (2017). Frictional strength of wet and dry montmorillonite. *Journal of Geophysical Research: Solid Earth*, *122*, 3392–3409. http://doi.org/10.1002/2016JB013658

Mu, C.-H., Angelier, J., Lee, J.-C., Chu, H.-T., & Dong, J.-J. (2011). Structure and Holocene evolution of an active creeping thrust fault: The Chihshang fault at Chinyuan (Taiwan). *Journal of Structural Geology*, *33*(4), 743–755. https://doi.org/10.1016/j.jsg.2011.01.015

Offler, R., & Prendergast, E. (1985). Significance of illite crystallinity and b_o values of K-white mica in lowgrade metamorphic rocks, North Hill End Synclinorium, New South Wales, Australia. *Mineralogical Magazine*, *49*(352), 357–364. https://doi.org/10.1180/minmag.1985.049.352.06

Ohl, M., Plümper, O., Chatzaras, V., Wallis, D., Vollmer, C., & Drury, M. (2020). Mechanisms of fault mirror formation and fault healing in carbonate rocks. *Earth and Planetary Science Letters*, *530*, 115886. https://doi.org/10.1016/j.epsl.2019.115886

Ozawa, K., & Takizawa, S. (2007). Amorphous material formed by the mechanochemical effect in natural pseudotachylyte of crushing origin: A case study of the Iida-Matsukawa fault, Nagano Prefecture, Central Japan. *Journal of Structural Geology*, *29*(11), 1855–1869. https://doi.org/10.1016/j.jsg.2007.08.008

Passchier, C. W. (1982). Pseudotachylyte and the development of ultramylonite bands in the Saint Barthélemy Massif, French Pyrenees. *Journal of Structural Geology*, *4*(1), 69–79. https://doi.org/10.1016/0191-8141(82)90008-6

Pec, M., Stünitz, H., Heilbronner, R., & Drury, M. (2016). Semi-brittle flow of granitoid fault rocks in experiments. *Journal of Geophysical Research: Solid Earth*, *38*, 200–221. https://doi.org/10.1016/j.jsg.2011.09.001

Pec, M., Stünitz, H., Heilbronner, R., Drury, M., & de Capitani, C. (2012). Origin of pseudotachylytes in slow creep experiments. *Earth and Planetary Science Letters*, *355-356*, 299–310. https://doi.org/10.1016/j.epsl.2012.09.004

Peterlechner, M., Waitz, T., & Karnthaler, H. P. (2009). Nanoscale amorphization of severely deformed NiTi shape memory alloys. *Scripta Materialia*, *60*(12), 1137–1140. https://doi.org/10.1016/j.scriptamat.2009.02.055

Pope, G. A. (1995). Newly discovered submicron-scale weathering in quartz: Geographical implications. *The Professional Geographer*, *47*(4), 375–387. https://doi.org/10.1111/j.0033-0124.1995.00375.x

Potysz, A., Grybos, M., Kierczak, J., Guibaud, G., Lens, P. N. L., & van Hullebusch, E. D. (2016). Bacterically-mediated weathering of crystalline and amorphous Cu-slags. *Applied Geochemistry*, *64*, 92–106. https://doi.org/10.1016/j.apgeochem.2015.07.011

Rowe, C. D., Lamothe, K., Rempe, M., Andrews, M., Mitchell, T. M., Di Toro, G., et al. (2019). Earthquake lubrication and healing explained by amorphous nanosilica. *Nature Communications*, *10*(1), 320. https://doi.org/10.1038/s41467-018-08238-y

Rutter, E. H., Maddock, R. H., Hall, S. H., & White, S. H. (1986). Comparative microstructures of natural and experimentally produced clay-bearing gault gouges. *Pure and Applied Geophysics*, *124*(1–2), 3–30. https://doi.org/10.1007/BF00875717

Sibson, R. H. (1975). Generation of pseudotachylyte by ancient seismic faulting. *Geophysical Journal International*, *43*(3), 775–794. https://doi.org/10.1111/j.1365-246X.1975.tb06195.x

Sibson, R. H. (2003). Thickness of the seismic slip zone. *Bulletin of the Seismological Society of America*, *93*(3), 1169–1178. https://doi.org/10.1785/0120020061

Solum, J. G., van der Pluijm, B. A., & Peacor, D. R. (2005). Neocrystallization, fabrics and age of clay minerals from an exposure of the Moab Fault, Utah. *Journal of Structure Geology*, *27*(9), 1563–1576. https://doi.org/10.1016/j.jsg.2005.05.002

Tamura, N. (2014). XMAS: A versatile tool for analyzing synchrotron X-ray micro-diffraction data. In G. E. Ice, & R. Barabash (Eds.), *Strain and Dislocation Gradients from Diffraction*, (pp. 125–155). Imperial College Press: London. https://doi.org/10.1142/9781908979636_0004

Tanikawa, W., & Shimamoto, T. (2006). Klinkenberg effect for gas permeability and its comparison to water permeability for porous sedimentary rocks. *Hydrology and Earth System Sciences Discussions*, *3*(4), 1315–1338. https://doi.org/10.5194/hessd-3-1315-2006

Tarling, M. S., & Rowe, C. D. (2016). Experimental slip distribution in lentils as an analog for scaly clay fabrics. *Geology*, *44*(3), 183–186. https://doi.org/10.1130/G37306.1

Thomas, M. Y., Avouac, J.-P., Gratier, J.-P., & Lee, J.-C. (2014). Lithological control on the deformation mechanism and the mode of fault slip on the Longitudinal Valley Fault, Taiwan. *Tectonophysics*, *632*, 48–63. https://doi.org/10.1016/j.tecto.2014.05.038

Tomita, K., Yamane, H., & Kawano, M. (1993). Synthesis of smectite from volcanic glass at low temperature. *Clays and Clay Materials*, *41*(6), 655–661. https://doi.org/10.1346/CCMN.1993.0410603

Toy, V. G., Mitchell, T. M., Druiventak, A., & Wirth, R. (2015). Crystallographic preferred orientations may develop in nanocrystalline materials on fault planes due to surface energy interactions. *Geochemistry, Geophysics, Geosystems*, *16*, 2549–2563. https://doi.org/10.1002/2015GC005857

Ueda, T., Ovata, M., Di Toro, D., Kanagawa, K., & Ozawa, K. (2008). Mantle earthquakes frozen in mylonitized ultramafic pseudotachylytes of spinel-lherzolite facies. *Geology*, *36*(8), 607–610. https://doi.org/10.1130/G24739A.1

Ufer, K., Kleeberg, R., Bergmann, J., & Dohrmann, R. (2012). Rietveld refinement of disordered Illite-Smectite mixed-layer structures by a recursive algorithm. II: Powder-pattern refinement and quantitative phase analysis. *Clays and Clay Minerals*, *60*(5), 535–552. https://doi.org/10.1346/CCMN.2012.0600508

Velde, B., & Vasseur, G. (1992). Estimation of the diagenetic smectite to illite transformation in time-temperature space. *American Mineralogist*, *77*(9–10), 967–976.

Verberne, B. A., Plümper, O., & Spiers, C. J. (2019). Nanocrystalline principal slip zone and their role in controlling crustal fault rheology. *Minerals*, *9*(6), 328. https://doi.org/10.3390/min9060328

Vrolijk, P., & van der Pluijm, B. A. (1999). Clay gouge. *Journal of Structural Geology*, *21*(8–9), 1039–1048. https://doi.org/10.1016/S0191-8141(99)00103-0

Wenk, H., Heidelbach, R., Chateigner, F., & Zontone, F. (1997). Laue orientation imaging. *Journal of Synchrotron Radiation*, *4*(2), 95–101. https://doi.org/10.1107/S090904959601432X

Wenk, H. R. (1978). Are Pseudotachylites products of fracture or fusion? *Geology*, *6*(8), 507–511. https://doi.org/10.1130/0091-7613(1978)6<507:APPOFO>2.0.CO;2

Wibberley, C. A. J. (2002). Hydraulic diffusivity of fault gouge zones and implications for thermal pressurization during seismic slip. *Earth, Planets and Space*, *54*(11), 1153–1171. https://doi.org/10.1186/BF03353317

Wu, Y.-M., Chen, Y.-G., Shin, T.-C., Kuochen, H., Hou, C.-S., Hu, J.-C., et al. (2006). Coseismic versus interseismic ground deformations, fault rupture inversion and segmentation revealed by 2003 M_w 6.8 Chengkung earthquake in eastern Taiwan. *Geophysical Research Letters*, *33*, L02312. https://doi.org/10.1029/2005GL024711

Yielding, G., Freeman, B., & Needham, D. T. (1997). Quantitative fault seal prediction. *AAPG Bulletin*, *81*(6), 897–917.

Yu, S.-B., Chen, H.-Y., & Kuo, L.-C. (1997). Velocity field of GPS stations in the Taiwan area. *Tectonophysics*, *274*(1-3), 41–59. https://doi.org/10.1016/S0040-1951(96)00297-1

Yund, R. A., Blanpied, M. L., Tullis, T. E., & Weeks, J. D. (1990). Amorphous material in high strain experimental fault gouges. *Journal of Geophysical Research*, *95*(B10), 15,589–15,602. https://doi.org/10.1029/JB095iB10p15589

Zhao, S., Hahn, E. N., Kad, B., Remington, B. A., Wehrenberg, C. E., Bringa, E. M., & Meyers, M. A. (2016). Amorphization and nanocrystallization of silicon under shock compression. *Acta Materialia*, *103*, 519–533. https://doi.org/10.1016/j.actamat.2015.09.022

Zhu, C., Veblen, D. R., Blum, A. E., & Chipera, S. J. (2006). Naturally weathered feldspar surfaces in the Navajo Sandstone aquifer, Black Mesa, Arizona: electron microscopic characterization. *Geochimica et Cosmochimica Acta*, *70*(18), 4600–4616. https://doi.org/10.1016/j.gca.2006.07.013